LAAS Ionosphere Spatial Gradient Threat Model and Impact of LGF and Airborne Monitoring

Ming Luo, Sam Pullen, Jed Dennis, Hiroyuki Konno, Gang Xie, Todd Walter, and Per Enge
Stanford University

Seebany Datta-Barua
Boston College

Tom Dehel
FAA William J. Hughes Technical Center

ABSTRACT

The ionosphere spatial gradient and its temporal rate of change in the vicinity of a LAAS-equipped airport are likely to influence the architecture required to meet the Category II/III precision approach and landing requirements. An initial parametric analysis depicts the effects of ionosphere anomalies on the position error of users for the current Category I LAAS architecture. In the ionosphere threat model used by previous analyses, an ionosphere gradient travels towards the airport at approximately 110 m/s with a change in ionospheric delay of 6 meters over a 19-km width. When the LAAS Ground Facility (LGF) detects the ionospheric delay before it impacts the airplane, there is no error. In other cases, the accumulated error depends on the parameters of the ionospheric gradient. The previous analysis shows that, although LGF detection is extremely important, the current architecture may not be able to meet LAAS requirements [3, 11] under worst-case ionosphere conditions.

In this paper, the ionosphere threat model is reexamined based on WAAS and IGS data from the 6 April 2000 ionospheric event. The analysis of additional data provides more information than was previously available. As the first step of developing a specific, clear, and bounded threat space model, the FAA Key Technical Advisors (KTAs) reached a preliminary consensus in March 2003. The resulting threat space attempts to cover a range of possible ionospheric events in CONUS extrapolated from the previous linear-gradient model. Four parameters of the ionospheric wave front were identified: gradient slope (30 – 400 mm/km), gradient width (15 – 200 km), wave front speed (0 – 1000 m/s), and angle between the wave front motion and the airplane approach direction (0 – 360°).

The impact of potential ionosphere anomalies on LAAS users is simulated in range domain over this entire threat space. The dependence of the differential range error on the user-LGF separation is evaluated. The maximum differential range errors at 5 km of user-to-LGF separation are computed for four monitoring scenarios: (1) no monitoring; (2) LGF monitoring; (3) airborne monitoring; and (4) LGF and airborne monitoring. These simulations determine the fraction of the threat space in which the range error impact can be mitigated by LGF monitoring alone or by LGF and airborne monitoring together. Based on these results, the degree of importance of both LGF and airborne monitoring requirement are assessed. Data analysis of other ionosphere storms and position-domain anomaly simulations are also underway.

1.0 INTRODUCTION

The ionosphere is a dispersive medium located in the region of the upper atmosphere between about 50 km to about 1000 km above the earth [1]. The radiation of the sun produces free electrons and ions that cause phase advance and group delay to radio waves. As GPS signals traverse the ionosphere, they are delayed by an amount proportional to the total electron content (TEC). The state of the ionosphere is a function of intensity of solar activity, magnetic latitude, local time, and other factors. The error introduced by the ionosphere into the GPS signal is highly variable and difficult to model at the level of precision needed for LAAS. However, under nominal condition, the LAAS user differential error is small (less than 25 cm).

The possibility of extremely large ionosphere spatial gradients was originally discovered in the study of WAAS "supertruth" (post-processed, bias-corrected) data during ionosphere storm events at or near solar maximum (2000-2001). Most storm data behaves as expected when shown on a plot of differential ionosphere vertical delay vs. ionosphere pierce point (IPP) separation, meaning that typical spatial gradients are increased but are still acceptable for LAAS (in CONUS, a conservative one-sigma value for vertical ionosphere spatial decorrelation is about 5 mm/km [10]). However, the onset of a storm on 6 April 2000, as shown in Figure 1, included an odd "tail" in the upper left of large (6 – 8 meter) differential delays over surprisingly short IPP separations (under 20 km). The sharpest gradient at the tip of this tail is 6 m over 7 km. However, since the IPP moved in the opposite direction from the apparent ionosphere anomaly, our best

estimate of the "true" IPP separation is 19 km (more detailed data analysis on this ionospheric event can be found in [2]). This gradient translates into an ionosphere delay rate of change of approximately 316 mm/km, which is 63.2 times the typical one-sigma ionosphere vertical gradient value identified previously. Since a Gaussian extrapolation of the 5 mm/km one-sigma number does not come close to overbounding this extreme gradient, and because it is impractical to dramatically increase the broadcast one-sigma number without losing all system availability, we must treat this event as an anomaly and detect and exclude cases of it that lead to hazardous user errors.

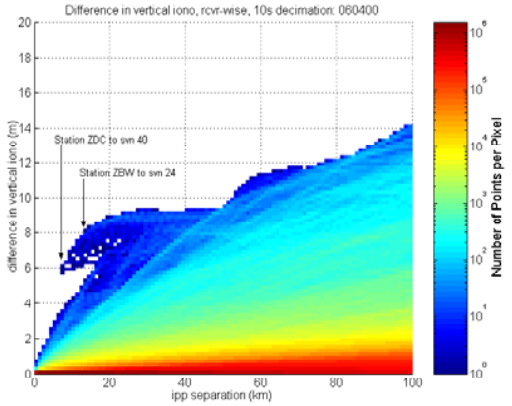

Figure 1: Ionospheric Spatial Anomaly Observed During 6 April 2000 Storm

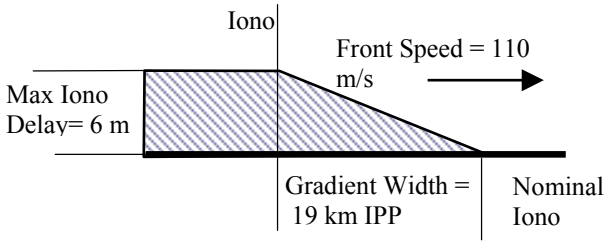

Figure 2: Simplified (Baseline) Model of Ionosphere Anomaly

Based on the WAAS supertruth data, the iono anomaly can be modeled as a semi-infinite "cloud" with a wave front pattern. Figure 2 shows the baseline model identified from the worst-case (sharpest gradient) point in the WAAS data shown previously, where the amplitude of the wave (high-to-low vertical delay difference) is 6 m, the width of the gradient is 19 km, and the wave moves forward at 110 km/s based on an average propagation speed estimated over the 90 minutes that the gradient is clearly visible moving approximately southward across the northeast quadrant of CONUS. The gradient itself is modeled as a linear change in vertical ionosphere delay between the "high" and "low" delay zones. This model of an example ionosphere gradient anomaly is called the "baseline" model in this paper.

It is important to estimate the impact of this type of anomaly on LAAS users. If both the user and the LAAS LGF observe the same ionospheric delay on a given GPS satellite, then there is no impact since the user error induced by the ionosphere will cancel out when the differential corrections broadcast by the LGF are applied. However, if the user and the LGF see different ionosphere delays, there will be some differential error. Given that this wave sweeps over a LAAS-equipped airport, the worst case from the aircraft's point of view is a wave front that approaches from directly behind an aircraft on approach and overtakes the ionospheric pierce point of an aircraft before the aircraft reaches its decision height (note that a typical jet aircraft final approach speed is about 70 m/s, which is slower than the baseline wave front model). After the wave front overtakes the aircraft, a differential range error builds up as a function of the rate of overtaking (in this case, 110 – 70 = 40 m/s) and the slope of the gradient (316 mm/km). Before the wave front reaches the corresponding LGF pierce point, there is no way for the LGF to observe (and thus be able to detect and exclude) the anomaly. The worst-case timing is that which leads to the maximum differential error (often this means the time immediately before LGF detection and exclusion) at the moment when the aircraft reaches the decision height for a particular approach (the point at which the tightest VAL applies). Note that this worst-case event and timing, if it ever were to occur, would only affect one aircraft. Other aircraft on the same approach would be spread out such that the wave front passage would create no significant hazard for them (VAL far from the decision height is higher than the error that could result from this anomaly [11]).

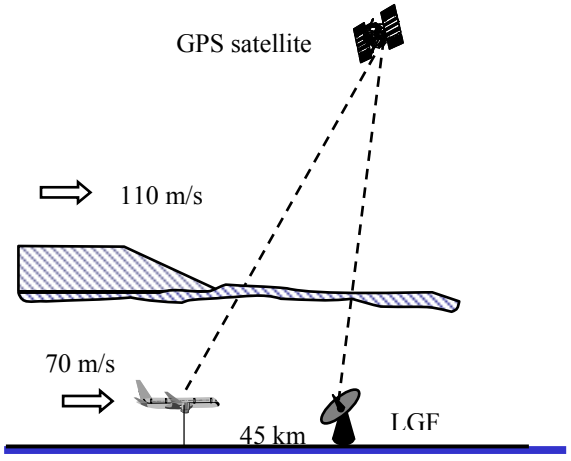

Figure 3: A "Near-Worst-Case" LAAS User Scenario

A "near-worst-case" scenario of this sort is sketched in Figure 3. In this scenario, the user is 45 km away (the

limit of LAAS VHF data broadcast coverage [3]) and is approaching the LGF at a speed of 70 m/s. The ionosphere front is behind the airplane and is moving in the same direction at a speed of 110 m/s. The ionosphere front is going to "catch" the airplane (reach the IPP between the aircraft and the GPS satellite), pass it, and eventually hit the IPP between the LGF and the satellite. The LGF "sees" the ionosphere from then on and gradually incorporates it into its differential corrections. The impact of this baseline ionosphere anomaly model on LAAS users was analyzed in detail in [4]. A sensitivity study can also be found in the same paper.

2.0 THREAT MODEL

Although the model based on WAAS supertruth data offers insight as to the likely behavior of abnormal ionosphere events, data from IGS and reference receiver sites provide more information than was previously available. Figure 4 shows the changes in ionospheric delay as measured by an NSTB site in Atlantic City, NJ, and several CORS sites in the mid Atlantic region. The small temporal difference of the drop, as observed from several sets of measurements, suggests the orientation of this "wall" in this localized region can be determined. For this data, as seen by receivers in this region, the ionospheric "wall" travels approximately 300 km in roughly 500 seconds, appearing to give it a speed of 600 m/s; since the satellite was moving against the direction of the wall movement, the satellite speed of 100 m/s (as discussed earlier) needs to be removed, leaving a net ionospheric wall speed of approximately 500 m/s. A similar analysis was done on CORS sites in the northeast, and there the ionospheric wall speed was estimated to be 380 m/s.

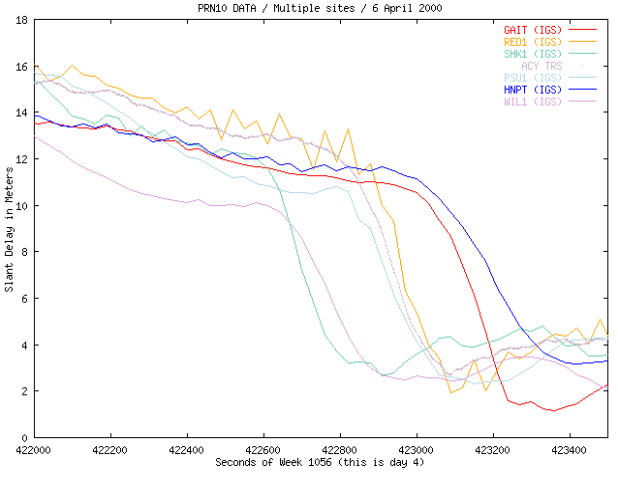

Figure 4: Drop in Ionospheric Delay at Multiple Sites Showing Motion of "Wall"

The earlier estimate of the wall gradient (slope) depended on the deduction of the speed of the wall from the separate observations of the wall in the Northeast (WAAS reference station in Boston), and the observation in the mid Atlantic (WAAS Reference Station in Washington, D.C.). The earlier estimate of the wall width was that the entire ionospheric change was observed over about 19 km; however, if the wall is moving much faster then the earlier estimate, then the width of the "wall" will be much larger (closer to 75 km), which may present a lesser threat to a LAAS installation.

The explanation for the difference in the results is that the earlier estimate of wall speed included the assumption that the wall moved continuously at the same speed from the Boston observation to the Washington observation. Because this analysis (using more-closely spaced observations) indicates that the speed at each end was much higher, the final element to be investigated is whether the wall speed changed in between the two measurements. In fact, for all the measurements to be consistent, the only apparent explanation is that the wall slowed or stopped somewhere in between the two spaced measurements (i.e., measurements in Boston and Washington). A search of the other available data showed that satellites which had IPPs moving over this central region showed a much slower drop of ionospheric delay, as would be expected from a stationary or slow moving wall with a width much greater than the earlier estimate of 19 km. The change in ionospheric delay is shown in Figure 5.

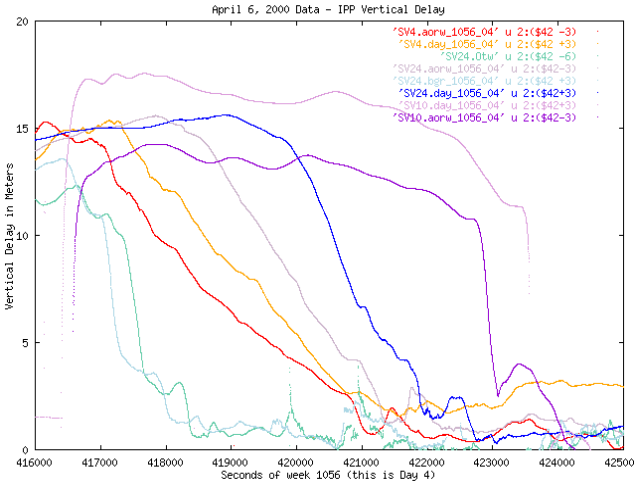

Figure 5: Measurements of Ionospheric Change From Multiple Sites

Figure 5 shows steep drops early (at about time 417, 500 s), and late (at about 423,000 s), however, the measurements over the intervening time do not show any evidence of a very narrow wall. It does get somewhat more complicated in that each satellite does move a

different angle through the wall, meaning that the satellite IPP maybe moving more parallel to the wall than perpendicular to the wall. However, in this case, all the measurements show that the wall was much wider than 19 km. Figure 6 shows the approximate locations of the satellite IPPs in relation to the wall when moving fast and slow. More details on the IGS data analysis of the 6 April 2000 event can be found in [5].

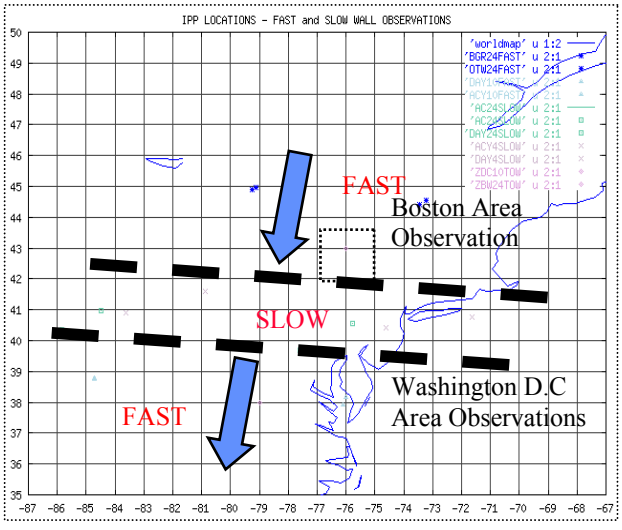

Figure 6: Approximate Ionospheric Wall Location (Where Moving Fast or Slow)

Figure 7 is similar in format to Figure 1 but was generated from US Naval Observatory IGS data on 6 April 2000 rather than WAAS supertruth data. Both reference sites are in the Washington. D.C. area. This plot shows typical ionosphere vertical spatial gradients during the time preceding and during the onset of the ionosphere storm, but there are a few outlier points in the lower left that apparently correspond to the time of the wave front passage (outlying points can also be seen for larger separations, as would be expected). Note that the y-axis is in units of 10^4 mm, or 10 m, so the top line represents a delay difference of 60 m.

A zoomed-in view lower-left corner of the above plot is shown in Figure 8. The largest gradient observed here is about 4.3 m over 15 km, which is similar to the 6 m over 19 km seen in the WAAS supertruth data from a nearby location. However, this 15-km width is the "raw" width and has not yet been corrected for IPP motion. Since this point is likely on the same satellite as that of the largest gradient in the WAAS data, accounting for IPP motion will likely increase the width by 10 – 12 km and make the gradient less sharp. Note that, even in this zone of anomalous points, only three points exist near the maximum gradient (IGS data points are separated by 30 seconds in time).

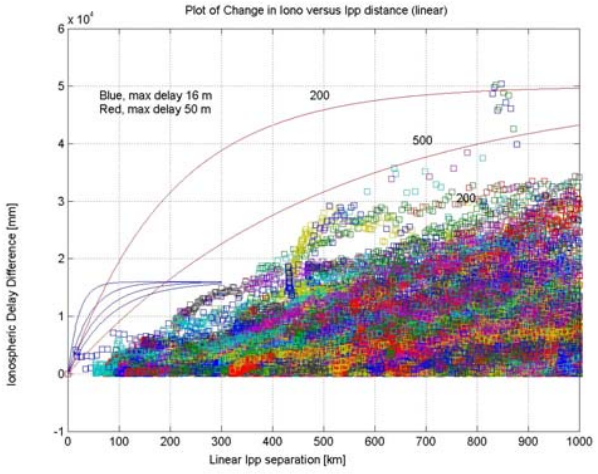

Figure 7: Ionosphere Differences from USNO IGS Data (6 April 2000 UTC, 30-sec Updates Over 24 Hours)

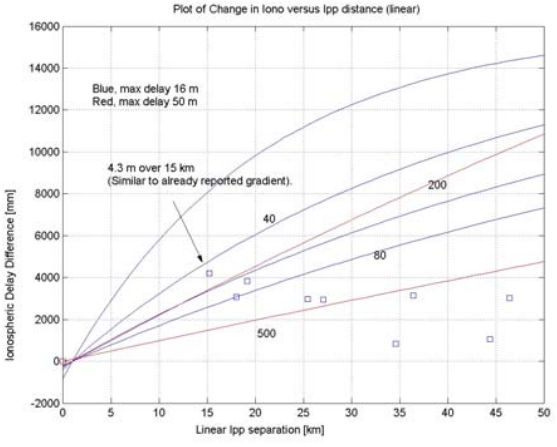

Figure 8: Zoom-In on Anomalous Short-Baseline Points in USNO IGS Data (6 April 2000 UTC)

In order to better capture the range of possible ionosphere wave front characteristics, the linear gradient model shown as Figure 9 is redefined with three parameters: velocity (v), gradient width (w), and gradient slope (g). The total delay difference (D) is then given by: $D = wg$. Velocity includes both scalar speed ($|v|$) and direction. For direction, we define a velocity vector along the aircraft approach direction (the worst case from the last slide) as 0 degrees. While this linear model is an approximation of reality and is likely to be conservative, it provides a reasonable basis for sensitivity studies of the threat posed by a wide variety of potential ionosphere anomalies.

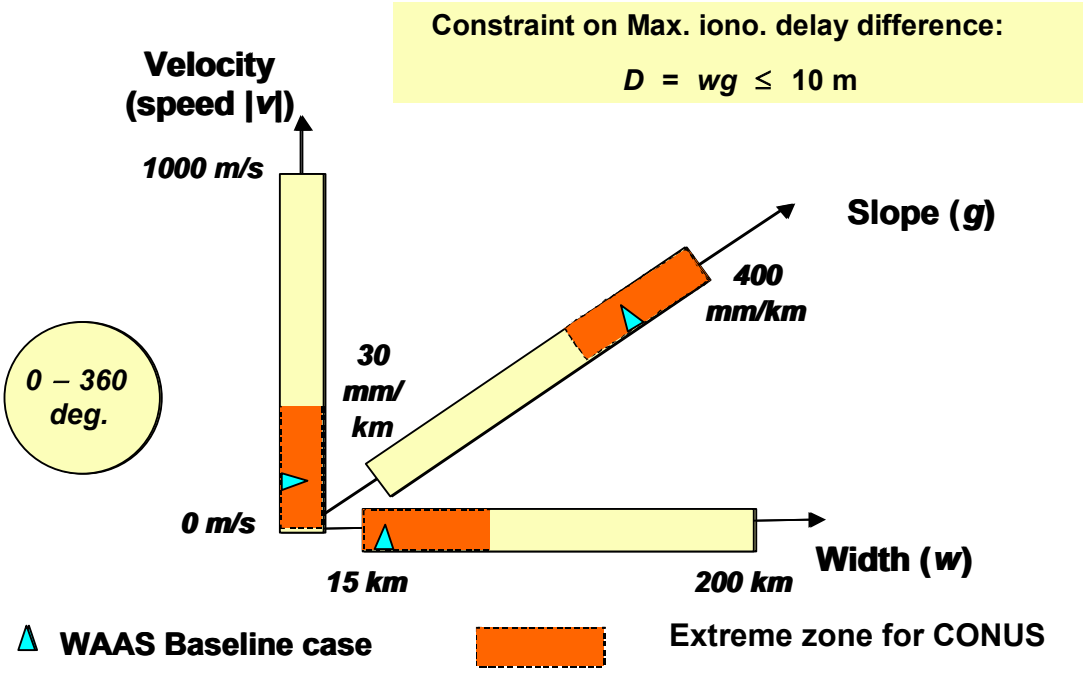

Figure 9: Ionosphere Spatial Anomaly Threat Space

Based on the anomaly data analyzed thus far, a threat space has been developed by the LAAS Key Technical Advisors to identify the upper and lower bounds on each of the four variables in the threat space, as shown in Figure 9. For the gradient slope, the lower bound of 30 mm/km represents 6 times the one-sigma value expected in CONUS during active ionosphere periods (5 mm/km), and the upper bound represents a hypothetical 6 meters of vertical delay difference over the minimum gradient width of 15 km. Note that there is an external constraint that the total vertical ionosphere delay difference D must be no greater than 10 meters (the maximum delay difference considered possible over the short baselines considered here). Thus, points nominally within the 4-D hypercube of this threat space that have $wg > 10$ m are excluded from the threat space. This threat space is used in all of the simulation results in this paper.

The red (darker) boxes in Figure 9 approximately represent the segment of the threat model that has been called into question based on the FAATC IGS data analysis shown in Figures 4 - 6. These results suggest that, when the very large 6 m/19 km gradient was observed in the 6 April 2000 data, the instantaneous ionosphere wave front speed was closer to 500 m/s rather than the 110 m/s average speed over 1.5 hours. This would have the effect of making the gradient slope look larger than it really is from the point of view of a stationary receiver. The question is whether a 6 m/19 km gradient in static ionosphere delay could exist with a wave front speed as low as 110 m/s, as implied in the baseline threat model (the baseline model parameters are shown as blue triangles in Figure 9). We do not have sufficient data to answer this question at present, but a "reduced" threat model (without the sections shown in red on the slide) may be more physically realistic, at least for CONUS. Study of ionosphere data for other known ionospheric storm days is underway to attempt to better answer this question and better define the parameters of the red (dark) zones, if they can be justified. In the meantime, the full threat model (including the dark zones) is used in the simulations reported in this paper. Note that the threat model definition also constrains the total amplitude (slope × width) of the vertical ionospheric delay gradient to be no greater than 10 meters. The points on the slope and width plot that translate into total delays exceeding 10-meters (i.e., are above the red plane in the plot) are not part of the threat model, even though they are included in this plot.

3.0 IMPACT IN RANGE DOMAIN

Range domain simulations (focusing on the impact of ionosphere anomalies on a single GPS satellite measurement) have been performed within the entire threat space defined in Section 2.0. The degree of hazard is determined under four different LAAS scenarios, respectively:

(1) No LGF or airborne monitoring
(2) LGF, but no airborne, monitoring
(3) Airborne, but no LGF, monitoring (primarily of theoretical interest)
(4) LGF and airborne monitoring

For each scenario, range-domain differential (user-minus-LGF) error simulations are conducted, and the worst-case errors are tabulated for further study. Histograms of error probabilities are also generated and compared at the end of this section. In order to clarify the ambiguity in the y-axis labels in the upcoming figures, note that only range domain simulation results are described in this section. While various terms are used for simplification (e.g., "user error", "diff. error", "vertical error", etc.), they all refer to differential zenith (vertical, as opposed to slant) ionosphere range error. Obliquity factors and satellite geometry are not included in the results in this section. Position-domain results are in Section 4.0.

3.1 Results with No Monitoring

In the scenario illustrated in Figure 3, the range-domain differential error that the user observes builds up as the error enters its carrier-smoothing filter:

$$PR_s(k) = \frac{1}{N_s} PR(k) + \frac{N_s - 1}{N_s}[PR_s(k-1) + \phi(k) - \phi(k-1)] \quad (1)$$

where:

$PR_s(k)$ = Carrier Smoothed Code (CSC) at k^{th} epoch.

$PR(k)$ = raw pseudorange measurement at k^{th} epoch.

N_s = Smoothing filter time constant (200 epochs, or 100 seconds)

$\phi(k)$ = carrier phase at k^{th} epoch.

These simulations assume that both the airborne user and the LGF apply first-order carrier smoothing using (1) with the same smoothing time constant of 100 seconds, as implied in [3, 12].

Figure 10 illustrates how, for the baseline ionosphere anomaly model, the differential error emerges as the airplane approaches a LAAS-equipped airport. The upper subplot shows the position of the airplane and the "leading edge" (the point at which the gradient begins to occur) of the ionosphere anomaly wave front relative to the LGF. The blue line represents the wave front position. The red line indicates the airplane position. The *x*-axis is the time of the airplane approach at a 2 Hz rate i.e., 2 epochs per second. The lower subplot shows the differential range error (which builds up during LGF and aircraft carrier smoothing based on vertical ionosphere delay differences) during the airplane approach. Assume that, at time zero of the simulation, the airplane is at 45 km away from the LGF (the edge of LAAS VHF data broadcast coverage), and the ionosphere wave front is just about to affect the airplane's IPP for a given GPS satellite. With a constant airplane approach speed of 70 m/s, it takes the airplane 1286 epochs (about 12 minutes) to complete the approach. At epoch 1143, the airplane reaches a point 5 km from the LGF, where it is assumed to reach the decision height for the approach in question (this is where the tightest vertical alert limit bound applies [11]).

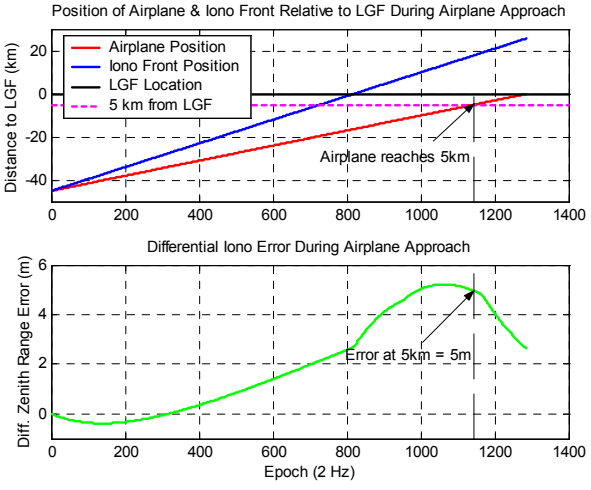

Figure 10: Differential Error during Airplane Approach, Baseline Model

At time zero, the airplane starts to be affected by the gradient portion of the wave front. Since the ionosphere event impacts carrier phase and pseudorange code measurements in opposite directions, the carrier-smoothed code has a negative trend first (the carrier updates dominate) before taking off to the positive direction (as the code error becomes more dominant). The error keeps increasing and would eventually reach a steady state a couple of time constants after the gradient portion of the wave front is passed. However, at epoch 818, the wave front reaches the LGF ionosphere pierce point for the satellite in question and starts to affect the measurements of reference stations in the similar fashion as it does to the airplane (a negative trend first, then a positive trend). As a result, the differential user error increases more dramatically at epoch 818 when the LGF measurements start to be impacted. It peaks at epoch 1063 (equivalent to an airplane position of 7.8 km from the LGF) and decreases from that point on. If the airplane continues to fly (instead of landing at epoch 1286), eventually the ionosphere impact on the user and the LGF would reach the same steady state and the differential error (the portion due to the ionospheric anomaly) would become zero. Note that the error of 5 m at 5 km is less than the

peak value of 5.5 m at 7.8 km. This indicates that the error can be worse if the distance from the decision height (approach threshold) to the LGF is greater than 5 km.

The scenario shown in Figure 10 assumed that the airplane and the leading edge of the wave front are both at 45 km away from the LGF at time zero. It is interesting to see how varying the initial position (but keeping the airplane and the wave front at the same location at the beginning of the simulation) affects the resulting differential errors. Figure 11 shows eight curves, each representing different initial positions from 10 km to 250 km from the LGF. The black curve represents the baseline case from Figure 10, corresponding to an initial position of 45 km. As can be seen, when the airplane and the wave front start far away from the LGF, there is more time for the wave front impact to fully develop; therefore the maximum user differential range error becomes greater (with the upper bound at about 7 m). However, because the effect on both the airplane and LGF approaches steady state (where both the LGF and aircraft see the same ionosphere delay) in those cases, the differential error at 5 km decreases (i.e., the point of maximum differential error has passed). When the airplane and the wave front start at a position closer to the LGF, there is not enough time for the full impact of the wave front to develop before the aircraft reaches the end of its approach. Thus, the resulting differential range error is also small. Note that there is a unique initial position of the airplane and the LGF that maximizes the differential error at 5 km.

To compare the range error at 5 km and the maximum error during each approach, the differential error at 5 km vs. initial aircraft (and wave front leading edge) position is plotted as the blue curve in Figure 12. It peaks at 5 m when the initial position of the airplane and LGF is about 45 km (which, coincidentally, is the baseline threat model). The maximum error along each approach is also plotted as the red curve. As discussed earlier, the maximum error increases as the initial position gets further from the LGF. It approaches about 7 m when the initial position gets to 80 km and beyond. Clearly, the 5 km constraint makes the possible impact smaller than what it would be in the worst case (for an unconstrained LGF-to-threshold separation). The good news is that even if this siting constraint is removed, the maximum error has an upper bound (about 7 m with the baseline ionosphere model). The fact that the effect of ionosphere spatial anomalies does not grow indefinitely with LGF separation is important when we consider approaches to alternate airports perhaps as far as 60 nautical miles away. Unlike ephemeris failures (see [14]), the impact of ionospheric anomalies reaches an upper limit and does not get worse with additional separation (although the impact of $\sigma_{vert\_iono\_gradient}$ on VPL does continue to grow.

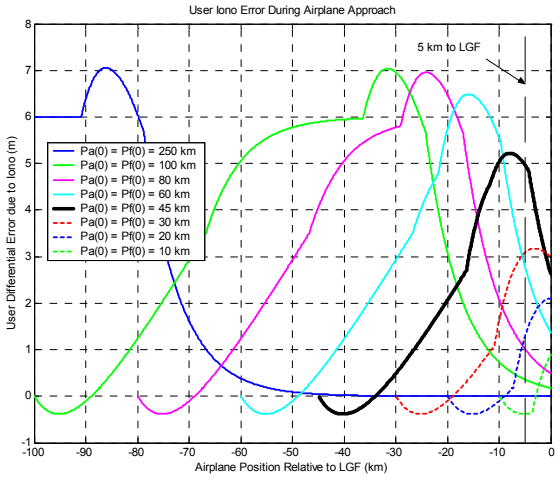

Figure 11: Differential Error During Airplane Approaches vs. Initial Position

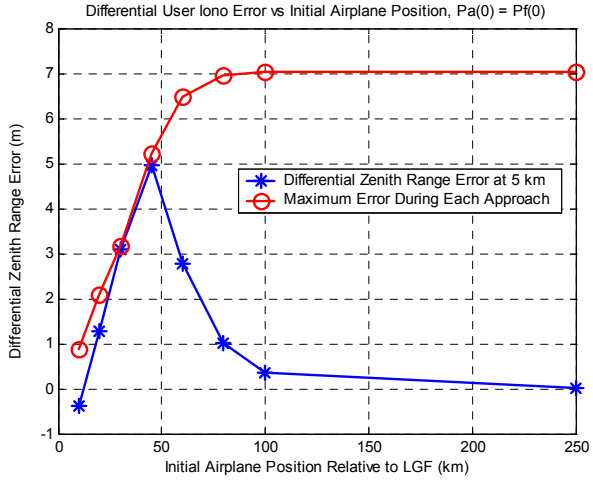

Figure 12: Comparison between Differential Error at 5 km and Maximum Error During Each Approach

In Figure 11, the initial position of the airplane and the LGF are kept the same. In other words, the wave front always just starts to overtake the airplane at time zero of the simulation. To conduct a more complete search, the two initial positions are allowed to vary independently. The range of initial airplane positions considered is from 6 km to 250 km. The initial ionospheric front position varies from that of the airplane position to 1.6 times that of the airplane position. Given that the airplane flies at 70 m/s and the ionospheric front moves at 110 m/s (for the baseline threat scenario considered here), the wave front cannot ever catch the plane if it starts at a position farther away than 1.6 times the initial airplane position. Therefore, the search space

considered here covers all possible combinations of the two initial positions.

The differential zenith range error over this entire range of initial positions is shown in Figure 13. Pf(0) denotes the initial ionospheric front position, and Pa(0) is the initial airplane position. The *x*-axis is the initial airplane position Pa(0), and the *y*-axis is the ratio between the initial ionospheric position and the airplane position, i.e., Pf(0) / Pa(0). As can be seen, the maximum error at 5 km is about 5 m. For each initial airplane position, there is an initial ionospheric front position that maximizes the error at 5 km. It confirms that the further the approach decision height is from the LGF, the greater the maximum differential error would be. As shown before, the upper-bound error is about 7 m for the baseline threat model.

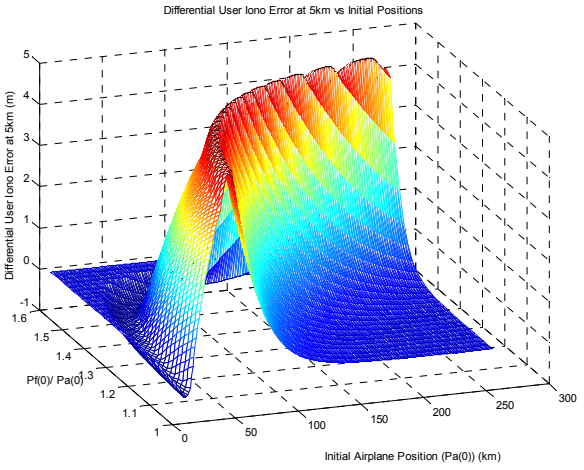

Figure 13: Differential Zenith Range Error at 5 km vs. Initial Airplane and Ionosphere Front Position (Complete Search of Baseline Case)

To illustrate further how the differential error depends on the distance of the approach threshold (decision height) from the LGF, four examples of the baseline anomaly case are plotted on Figure 14. Each subplot represents a decision distance (the separation between the LGF and the point on the approach associated with the decision height) of 1 km, 5 km, 10 km, and 50 km, respectively. Clearly, the larger the decision distance, the greater the peak differential error. Also, as this distance increases, the range of aircraft and wave front starting positions that lead to significant peak differential errors grows significantly, as shown in the lower-right plot (for 50 km).

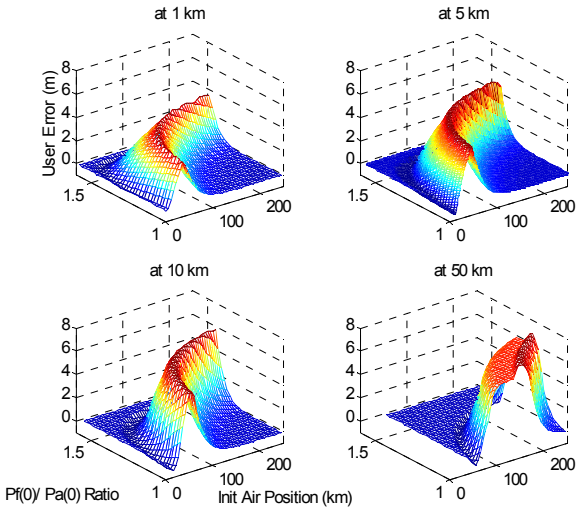

Figure 14: Impact of Variation in LGF – DH Separation (Baseline Case)

The maximum differential zenith ionospheric range error is plotted as a function of LGF-to-threshold (DH) separation distance in Figure 15 (for the baseline anomaly model). Again, it can be seen that the maximum user error increases as the decision distance increases. Between 1 and 10 km, the increase is almost linear, which means that roughly the same trend applies to ionospheric anomalies as to ephemeris failures (which are covered by ephemeris protection level calculations). Thus, these two anomalies have a similar impact on LAAS siting. Beyond 10 km, the ionospheric anomaly impact asymptotes off to an upper bound of about 7 m, whereas the impact of ephemeris failures keeps growing linearly with separation distance [14].

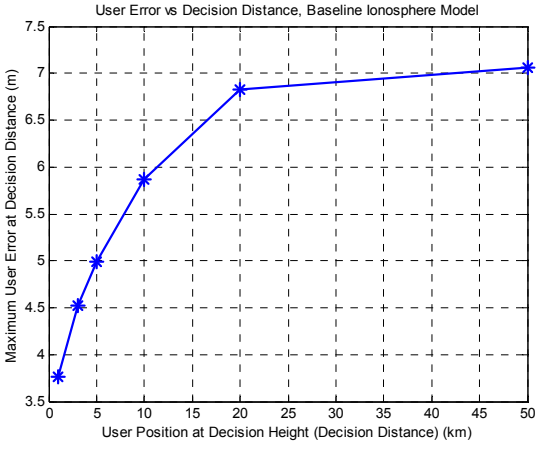

Figure 15: Maximum Differential Zenith Range Error vs. LGF – DH Separation (Baseline Case)

It is not clear what combination of ionospheric threat model parameters is more or less likely to happen (or has

happened). In order to illustrate some examples, four cases are constructed as follows:

Table 1: Four Example Ionosphere Spatial Anomaly Cases

Case #	Description	Slope (mm/km)	Width (km)	Speed (m/s)
1	The current baseline case	316	19	110
2	Baseline case with faster wave speed	316	19	500
3	More gentle (but still anomalous) gradient with baseline speed	100	100	110
4	More gentle (but still anomalous) gradient with faster speed	100	100	500

The differential zenith range error at 5 km for these four cases are compared in Figure 16 as functions of aircraft and wave front initial position. It appears that high wave front speed cases (#2 and #4) result in less differential error than the low-speed cases (#1 and #3). Also, a steeper gradient with shorter width (case #1, baseline) leads to larger errors than a flatter gradient with larger width (Case #3). This is important because, as pointed previously, the baseline case may be physically impractical, and less-severe gradients moving more rapidly (such as in case #4) may be more likely in practice.

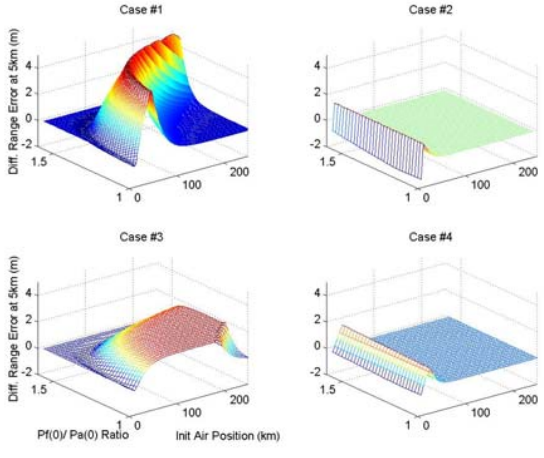

Figure 16: Comparison among Four Example Ionosphere Anomaly Cases

Although it is intuitive that the worst anomaly scenario for LAAS occurs when the wave front moves directly behind the approaching airplane. It is useful to see how the ionospheric impact depends on the wave front moving direction (relative to the airplane approach). Figure 17 shows differential zenith range errors 5 km from the LGF for the baseline anomaly model but with four different wave front velocity vector angles (relative to the approaching aircraft) of 0, 30, 60, and 90 degrees, respectively. It confirms our expectation that the worst direction is when the ionospheric front approaches from directly behind the airplane, i.e., the angle = 0 degree. That is because when the angle moves further from zero, the time gap between when the airplane sees the iono front and when the LGF sees it gets shorter. As an extreme example, at 90 degrees, the ionospheric front always impact the airplane and the LGF in the same way and at the same time; therefore the differential error is always zero. Note that with LGF monitoring, those wave fronts with angles of 90 to 270 degrees would be detected and excluded before the aircraft is impacted (since they affect the LGF first). Thus, these cases are not of concern for LAAS.

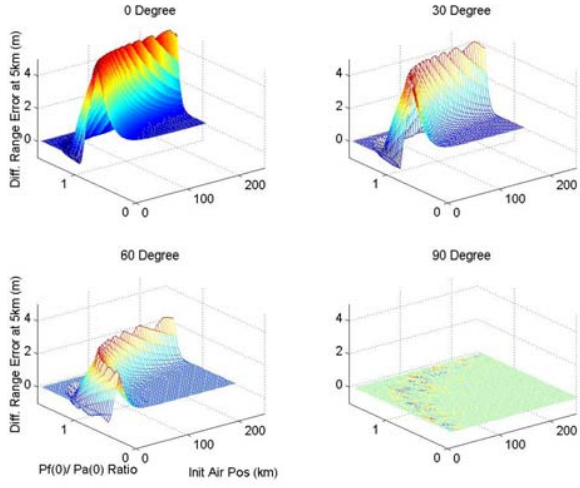

Figure 17: Comparison among Wave Front Approach Directions

Figure 18 shows all the worst differential zenith range errors at 5 km within the threat space for a constant (fixed) wave front speed of 110 m/s (the baseline speed). As mentioned previously, all of the points that give maximum ionosphere gradient amplitudes of greater than 10 meters are not in the threat space and are discarded (they show up on the plot as having zero differential error). Note that, for each gradient width, the differential (range-domain) error grows proportionately with gradient slope. When the width is small (< 50 km), the error also increases with increasing width. However, when the

width is large (greater than 50 km), the error becomes approximately constant (it is no longer sensitive to width). The maximum error is about 7 m, which happens at the corner of highest possible slope (400 mm/km) and small width (25 km, which is just larger than the 20-km minimum of this plot).

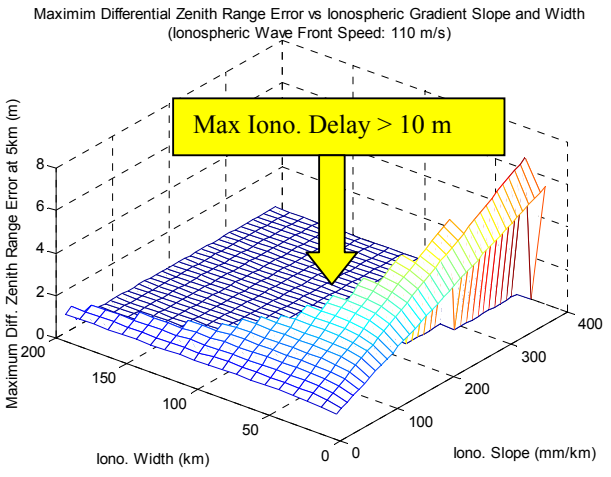

Figure 18: Range Error at 5 km vs Iono Slope and width

Figure 19 illustrates how changing the ionosphere wave front speed affects the maximum differential (vertical) range error. Cases with four different speeds (100, 300, 500,and 900 m/s) are plotted and compared. Generally, all other things being equal, the differential range error decreases as the ionospheric speed increases. Again, this is important because of the suggestion that, in practice, higher speeds are more likely if significant ionosphere anomalies occur.

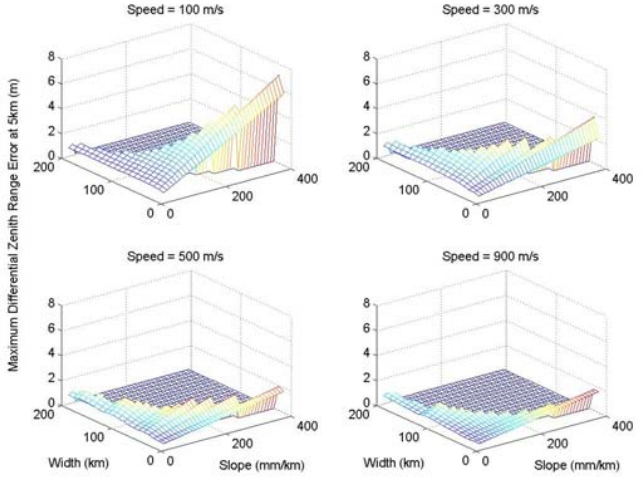

Figure 19: Maximum Differential Zenith Range Error at 5 km vs. Ionosphere Speed

In order to present all the cases in the threat space together, a summary plot is generated as shown in Figure 20. Each of the nine subplots represents one ionospheric speed from 100 to 900 m/s. The *x*-axis represents ionospheric wave front gradient width. Each color represents one ionospheric slope for the given width. Although the ionospheric slope information is blended in and is hard to read, the results for all ionospheric slopes in the threat space are included in each subplot. This figure confirms that higher ionospheric wave front speeds generally give smaller differential range errors. In particular, the cases of greatest concern for the no-monitoring scenario are those with slow wave front speeds and very sharp gradients (small width, high slope). Again, based on the FAATC data from the 6 April 2000 anomaly, these may be the least likely to occur.

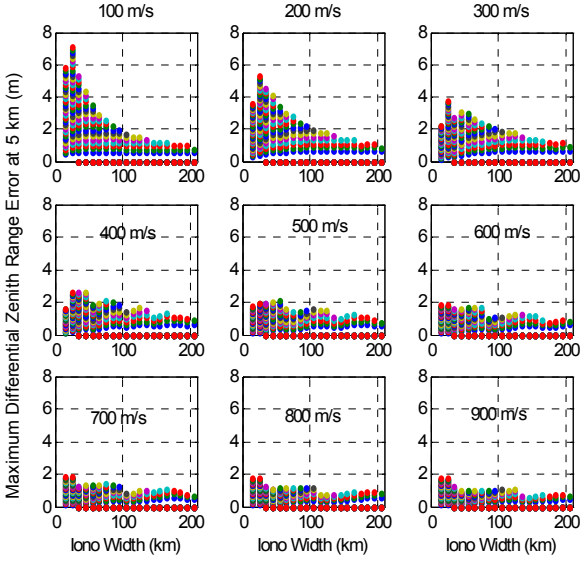

Figure 20: Differential Range Error Summary Plots With No Monitoring

Table 2 summarizes the worst-case (largest maximum differential range error) ionosphere anomaly parameters for the range of possible ionospheric wave front speeds shown in Figure 19. Note again that wave front speed is the most sensitive parameter – the maximum error decreases markedly as the ionosphere speed increases. The worst-case gradient is generally the maximum of 400 mm/km, although that is not always the case, and the worst-case gradient width is usually small but not always the smallest possible (15 km). The worst-case error of 7.1 meters occurs only for the segment of the threat space that is likely to be the least (largest gradient, small width, but slow wave front speed).

Table 2: Summary of Worst-Case Anomalies with No Monitoring

Iono. Front Speed (m/s)	Gradient Slope (mm/km)	Gradient Width (km)	Gradient Direction (deg.)	Worst-Case Diff. Range Error (m)
100	400	25	0	7.1
200	400	25	0	5.3
300	400	25	0	3.7
400	280	35	0	2.6
500	180	55	0	2.1
600	400	15	0	1.8
700	400	15	0	1.8
800	400	15	0	1.7
900	400	15	0	1.7

3.2 Results with LGF Monitoring

3.2.1 LGF Detection Capability

Given the ionosphere anomaly scenario shown in Figure 2, the LGF will be affected by the ionosphere front at some point during an approach. Once it is affected, one or more of the existing LGF integrity monitors may issue an alert despite not being designed specifically to detect this anomaly. In order to quantify this, we used the Stanford Integrity Monitor Testbed (IMT), an LGF prototype developed at Stanford University, to simulate the detection ability of the LGF. The IMT consists of various monitors to address integrity concerns such as satellite signal failures, ephemeris anomalies, receiver problems, RF interference, etc. Though each monitor was designed to target different failure modes, it was found that the multiple monitors of the IMT are sensitive to more than one type of anomaly, and several of them can detect the ionosphere spatial gradient modeled here. A brief description of those monitors is given in this section. More detailed IMT descriptions and algorithms can be found in [6,7,8].

MQM (*Measurement Quality Monitoring)*: This function is designed to detect sudden jumps or rapid acceleration in pseudorange and carrier phase measurements. Before carrier smoothing occurs on each epoch, the last 10 epochs (5 seconds) of carrier phase measurements of all ranging sources being tracked are used to fit the following 2nd-order model:

$$\phi^* = \phi_0^* + \frac{d\phi^*}{dt}\Delta t + \frac{d^2\phi^*}{dt^2}\frac{\Delta t^2}{2}; \qquad (2)$$

where:

$$\phi^* = \phi - \phi^{corr} - \phi^{ave} = \hat{\phi} - \phi^{ave}\ ; \qquad (3)$$

$$\phi^{ave} = \frac{1}{N_c}\sum_{i=1}^{N_c}\phi_i\ ; \qquad (4)$$

$$\phi^{corr} = R^{SV} + \tau^{SV}\ ; \qquad (5)$$

and where N_c is the number of satellites in the "common set" across the three IMT reference receivers, and R^{SV} and τ^{SV} are the user-to-satellite range and satellite clock corrections, respectively. Three test statistics are defined:

$$Step\ test \equiv \phi^*_{meas} - \phi^*_{pred}\ ; \qquad (6)$$

$$Ramp\ test \equiv \frac{d\phi^*}{dt}\ ; \qquad (7)$$

$$Acceleration\ test \equiv \frac{d^2\phi^*}{dt^2}; \qquad (8)$$

where ϕ^*_{meas} is the computed value of ϕ^* at the current epoch, and ϕ^*_{pred} is the value computed from (2) based on the coefficients ϕ^*_0, $\frac{d\phi^*}{dt}$, and $\frac{d^2\phi^*}{dt^2}$, which are computed from a least-squares fit to the last 10 phase measurements (taken over 5 seconds).

After smoothing is completed on a given epoch, anther test statistics, the MQM innovation is computed to detect unusual pseudorange deviations:

$$Inno(k) \equiv PR(k) - \left(PR_S(k-1) + \phi(k) - \phi(k-1)\right) \qquad (9)$$

Code-Carrier Divergence: This function was designed to address potential satellite failures that cause code-carrier divergence but will also detect unusual divergence due to the ionosphere. There are several versions of this monitor. Geometric Moving Averaging (GMA) is a traditional approach to sequential estimation of the apparent code-minus-carrier divergence rate, and the Cumulative Sum or CUSUM method modifies the standard CUSUM technique to produce an improved algorithm. Both methods will be briefly described here, and more detailed information can be found in [8].

GMA algorithm: The raw observable code-minus-carrier (denoted as z) is fed into a time-varying filter:

$$d_k = \frac{\tau_d(k)-T}{\tau_d(k)} d_{k-1} + \frac{1}{\tau_d(k)}(z_k - z_{k-1})$$
$$\text{where} \quad \tau_d(k) = \begin{cases} kT, & kT < \tau_{d\max} \\ \tau_{d\max}, & kT \geq \tau_{d\max} \end{cases} \quad (10)$$

where k is the epoch index, T_s = 0.5 seconds is the IMT GPS measurement update rate, τ_{dmax} = 200 seconds is the time constant of averaging, and z is the raw code-minus-carrier observable at each epoch. When a large ionospheric anomaly occurs, the averaged code-minus-carrier will differ from its nominal distribution, and an alert will be issued if the value exceeds a pre-set threshold. The GMA monitor gives low-noise divergence estimates by averaging multipath differences. Though this method is very stable, the detection of ionospheric gradient $\dot{I}$ can be quite slow, particularly when the gradient is relatively small.

CUSUM Algorithm: The Cumulative Sum (CUSUM) method has the theoretically minimal time-to-detect of a change in the parameters of a random process under certain assumptions. Consider a sequence of independent Gaussian random variables $x(k)$ with a probability density function (PDF) as follows:

$$p_u(x) = \frac{1}{\sqrt{2\pi}\,\sigma} e^{-\frac{(x-\mu)^2}{2\sigma^2}} \quad (11)$$

Its mean μ is equal to μ_0, called in-control-mean, in nominal case, and is shifted to out-of-control μ_1 when some failure happens in the random process, as illustrated in Figure 21. Its variance σ^2 is assumed to be a known constant and does not change before and after the failure.

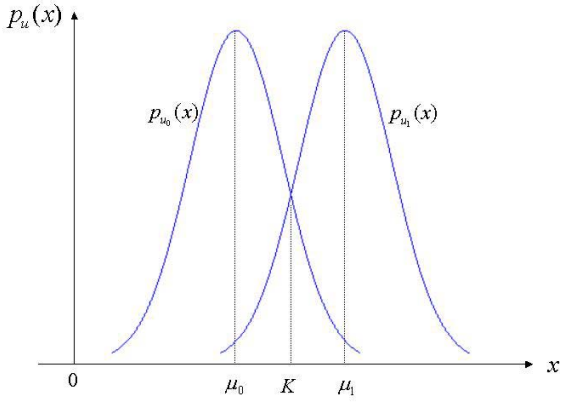

Figure 21: The PDF of a Gaussian Random Process with Mean μ_0 and μ_1

In the CUSUM algorithm that targets at detecting changes in mean μ, a log-likelihood ratio $s(k)$ is first defined as the ratio of the probability with x at $x(k)$ if $\mu = \mu_1$ to the probability if $\mu = \mu_0$, i.e., (10)

$$s(k) = \ln \frac{p_{\mu_1}(x = x(k))}{p_{\mu_0}(x = x(k))} = \frac{\mu_1 - \mu_0}{\sigma^2}(x(k) - K) \quad (12)$$

where the constant windowing factor K is the middle point between two means. The CUSUM method then accumulates information of the past observations by summing up $s(k)$ together:

$$C^+(k) = \sum_{i=1}^{k} s(k) = C^+(k-1) + s(k) = \left[C^+(k-1) + \frac{\mu_1 - \mu_0}{\sigma^2}(x(k) - K) \right]^+ \quad (13)$$

where the superscript "+" indicates that an h/2 Fast Initial Response (FIR) CUSUM that is used to detect positive mean jumps (i.e., $\mu_1 > \mu_0$) resets $C^+(k)$ to h/2 if $C^+(k) < 0$. If $C^+(k) \geq h$, the hypothesis of $\mu = \mu_1$ is valid and the failure is detected. The threshold h can be computed by using numerical search from the Markov Chain model of the CUSUM. Similarly, , $C^-(k)$ used to detect negative mean changes, need be implemented in parallel.

The CUSUM can be applied to fast detect relatively small but hazardous ionospheric gradients. The input to the CUSUM is the raw divergence $[z(k) - z(k-1)]/2T_s$ k_0. The in-control-mean μ_0 of a potential ionospheric gradient is real-time estimated by the GMA method on the CUSUM input; while its out-of-control mean μ_1 is constructed to be $\mu_0 + V$, where elevation-dependent V can be regarded as the target magnitude of the ionospheric gradients that the CUSUM aims to detecting. The variance of the input is pre-computed based on the statistical analysis of nominal data sets.

Since each IMT monitor was designed to target different potential failure modes in LGF measurements, their times-to-detect vary with apparent ionospheric delay rate-of-change as well as elevation angle. An example failure test is shown in Figure 22. Different magnitudes of anomalous ionospheric gradients, every 0.001 m/s from 0.013 m/s to 0.022 m/s, were injected into the measurements of PRN 2 at 70° elevation and rising. The times to flag (here it is the earliest time to exclude any one of the three IMT receivers tracking PRN 2) for the four monitors were compared. Several points are missing for the acceleration-ramp-step and GMA method since they fail to reliably detect these small gradients. The figure clearly shows that the acceleration-ramp-step test can detect relatively large gradients as fast as in several seconds. The CUSUM method does not detect large failures as fast as the acceleration-ramp-step, but it is better than the innovation and GMA methods. The acceleration-ramp-step and CUSUM method together

give the best possible lower bounds on detection time. Thus, the overall time-to-detect by the LGF is shown by the blue line (circles) in Figure 23.

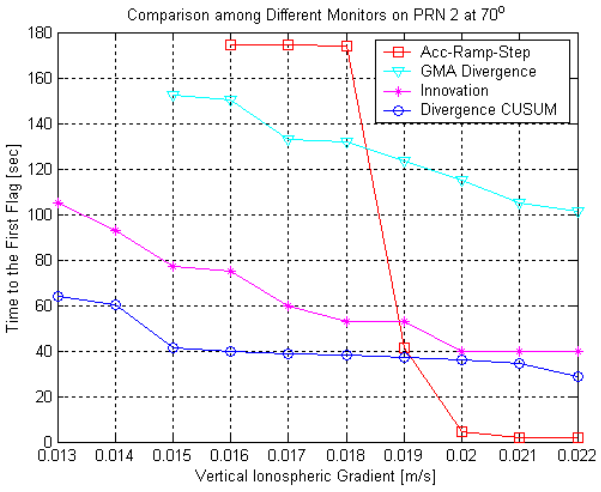

Figure 22: Failure Testing With Different Magnitudes of Ionospheric Gradients at 70° Elevation

Generally, MQM is the fastest when the apparent ionospheric rate is above a certain level (e.g., greater than 0.02 m/s for a high-elevation-angle satellite), and the CUSUM code-carrier divergence method is the best when the ionospheric rate is lower than this but still anomalous (e.g., between 0.01 and 0.02 m/s). For this analysis, it is assumed that no monitor detects ionosphere events with apparent ionosphere delay rates-of-change at the LGF lower than 0.01 m/s (this is likely required to meet the LGF continuity sub-allocation during non-hazardous ionosphere storms). Note that these test results may be strongly associated with factors unique to the Stanford IMT such as siting, antenna type, etc. The value used here may need to be adjusted to suit a different LGF system design. The time-to-detect for the airborne is also plotted in the same plot in red assuming that only the GMA algorithm is used there and that its performance is roughly equivalent to ground-based GMA.

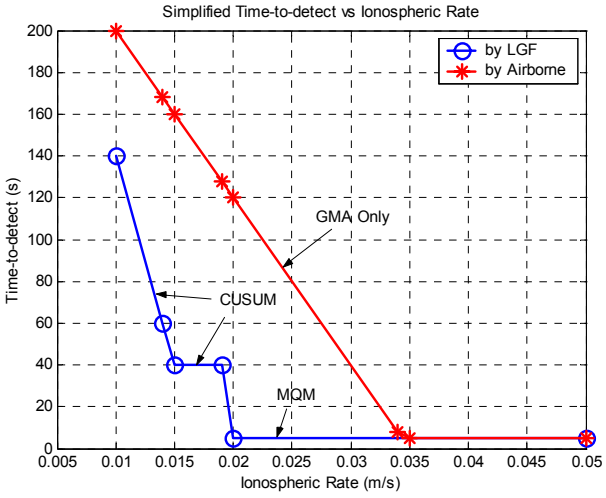

Figure 23: Time-to-detect vs. Ionosphere Delay Rate of Change (from Stanford IMT Failure Testing)

3.2.2 Simulation Results

The four example ionosphere anomaly cases shown in Table 1 and Figure 16 have been re-examined with LGF monitoring included. Case #1 (Slope = 316 mm/km, Width = 19 km, Speed = 110 m/s; baseline) and case #3 (Slope = 100 mm/km, Width = 100 km, Speed = 110 m/s) are shown in Figure 24 to compare the vertical ionospheric range errors with and without LGF monitoring in place. As soon as the LGF detects the anomaly, the affected measurement would be removed and would therefore no longer pose an integrity threat to the user. Clearly, LGF monitoring greatly reduces the differential range error for both cases. Although the error is greater in case #1 than in case #3 when no monitoring is applied, the residual error after LGF monitoring is smaller in case #1 than in case #3. This is due to the fact that, when the ionospheric gradient has a flatter slope, it has a better chance to "slip through" the MQM component of LGF detection (which, if it detects, will usually do so within 5 seconds of onset) and remain usable for longer, although the CUSUM monitor eventually detects it. Thus, the resulting differential error has more time to build up.

Figure 25 shows the impact of varying ionospheric anomaly slope and width for four different wave front speeds. Note that the two cases (1 and 3) shown in Figure 23 are only two data points in the plots of this format. As can be seen, when the ionospheric wave front speed is low, flatter-slope ionospheric events "sneak through" the fast MQM component of LGF detection and give the larger errors, although detection does occur later and limits the size of these errors to well below that of the no-monitoring case. When the wave front speed reaches 300 m/s, even flatter-slope cases would be detected by MQM because the apparent ionospheric delay rate-of-change at

the LGF exceeds 0.02 m/s (see Figures 22 and 23). However, when the speed grows to 500 m/s, the undetected differential user error becomes slightly larger because, even though LGF detection happens quickly, more error builds up at the aircraft before the wave front reaches the LGF. Above 500 m/s, these two effects more-or-less cancel out; thus the maximum ionospheric error stays about the same. Because of the complex interaction between aircraft impact and LGF detection, it is not surprising that the dependence of range error on ionosphere wave front speed is not monotonic.

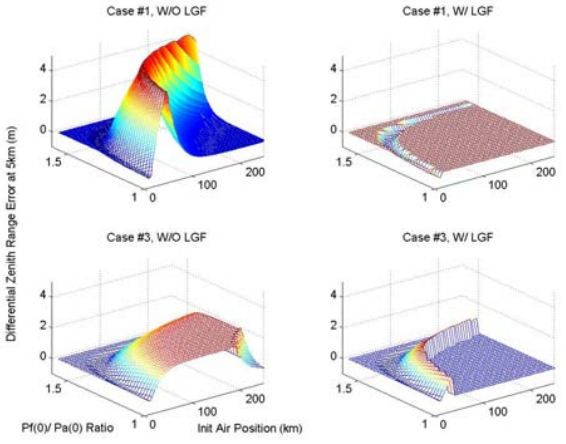

Figure 24: Example Cases 1 and 3 – Comparison with and without LGF Monitoring

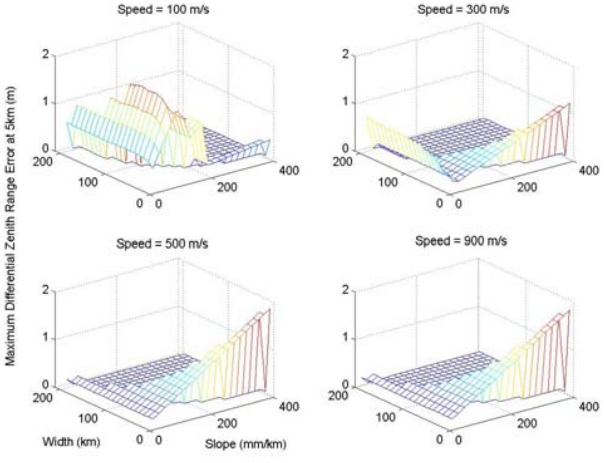

Figure 25: User Error over Ionosphere Threat Space (with LGF Monitoring)

Figure 26 summarizes all cases (over the entire threat space with a 5-km LGF-to-threshold separation and ionosphere wave front approach angle of 0 degrees) with LGF monitoring. The wave front speed of 200 m/s gives the smallest user range errors. When the speed exceeds 400 m/s (up to 1000 m/s, which is the maximum within the threat space), the situation remains relatively unchanged. Overall, with LGF monitoring in place, the maximum user range error is less than 2 m, which is a dramatic improvement over the no-monitoring scenario.

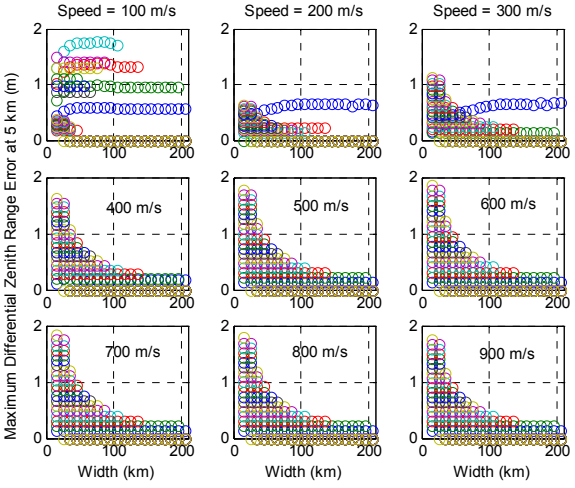

Figure 26: Summary Plots with LGF Monitoring

Table 3: Worst-Case Scenarios for Each Ionospheric Wave Front Speed With LGF Monitoring

Iono. Front Speed (m/s)	Gradient Slope (mm/km)	Gradient Width (km)	Gradient Direction (deg.)	Worst Diff. Range Error (m)
100	90	75	0	1.8
200	30	135	0	0.7
300	400	15	0	1.1
400	400	15	0	1.6
500	400	15	0	1.8
600	400	15	0	1.8
700	400	15	0	1.8
800	400	15	0	1.7
900	400	15	0	1.7

The maximum residual errors with various ionospheric speeds are summarized in Table 3. Unlike Table 2 for the no-monitoring case, the worst-case vertical differential range error with LGF monitoring is not a strong function of wave front speed and occasionally occurs (for a given speed) with lower gradients and larger widths. This is not surprising because the presence of LGF monitoring detects and excludes many of the worst-case anomalies before the user impact becomes significant. For higher wave front speeds, the worst-case anomaly is the largest and thinnest possible since the anomaly reaches the LGF quickly, and most of its range-error impact occurs before it can be

excluded. These cases are the ones that we expect to be helped the most by the addition of airborne monitoring.

3.3 Results with Airborne Monitoring

In this section, we assume that the airborne subsystem is equipped with a GMA-based code-carrier divergence monitor that has the same detection performance as the GMA monitor in the IMT; thus its time to detect ionosphere anomalies is indicated by the red curve in Figure 23. Note that this assumes that the same filtering time constant (200 seconds) is used in the airborne and that airborne errors are similar to those observed in the IMT. In reality, airborne multipath is likely to have a shorter correlation time constant; thus the airborne GMA monitor time constant can be reduced, which would allow faster detection in the airborne monitor. Since this potential benefit has not yet been quantified, we have conservatively assumed IMT-equivalent performance for airborne monitoring in this work.

The resulting differential zenith range errors for airborne monitoring (but no LGF monitoring) are plotted in Figure 27. As can be seen, the faster the ionosphere wave front moves, the greater the apparent ionospheric delay rate of change is at the aircraft; thus the aircraft detects and excludes the affected measurements earlier, which reduces the maximum residual user range error. The largest differential errors occur for low-speed, high-slope, and smaller width anomaly scenarios. Again, this is the part of the threat space that is least likely based on the data for the 6 April 2000 ionosphere anomaly reported above.

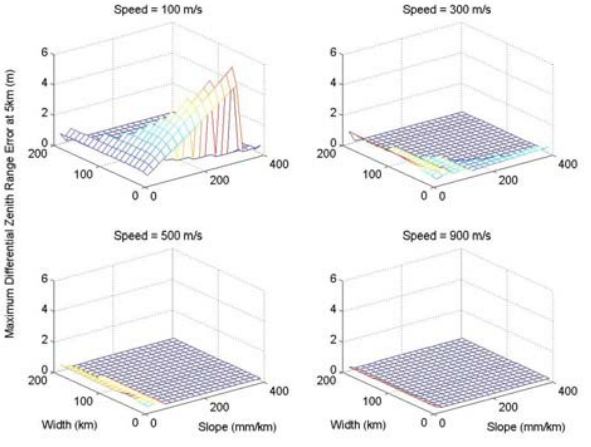

Figure 27: User Error over Ionosphere Threat Space (with Airborne Monitoring)

A more complete summary plot is shown in Figure 28. As noted previously, the airborne-only monitor is relatively ineffective for slow-speed anomalies because of the time it takes for the airborne monitor to detect the smaller apparent ionospheric delay rate of change. Thus, for a wave front speed of 100 m/s, the maximum error reaches about 6 m. However, when the wave front speed is equal to or greater than 400 m/s (which we think is the more likely anomaly scenario), the airborne monitor is extremely effective – the maximum range error is only about 0.5 m. For speeds much higher than 400 m/s, the maximum error is well below 0.5 meters and is essentially negligible.

By comparing the maximum range-domain errors with LGF detection (Figure 25) vs. airborne detection (Figure 27), it can be seen that LGF monitoring is relatively more effective against lower-speed event (300 m/s or lower) while the airborne monitoring is more effective toward higher-speed ones. Note that each approach has its relative advantages and disadvantages. The LGF has more comprehensive algorithms (including MQM and CUSUM) and observes a higher relative ionosphere wave front speed because it is not moving, whereas the aircraft is moving in the same direction as the anomaly in the threat scenarios of greatest concern (wave front relative approach direction = 0 degrees). On the other hand, the airborne monitor sees the ionospheric anomaly earlier that the LGF does.

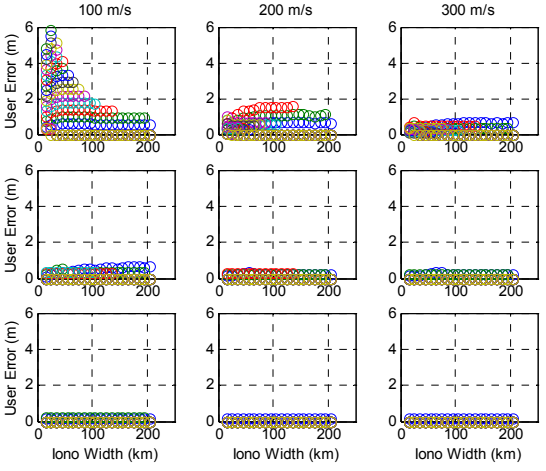

Figure 28: Summary Plots with Airborne Detection

In summary, LGF detection is better against low-speed anomalies, and it is generally better overall because it allows a differential range error no greater than 2 meters for any case within the ionospheric threat space. This 2-meter upper bound is likely to be sufficient for operations up to and including Category I precision approaches, but this is a preliminary conclusion only. Airborne monitoring is better vs. higher-speed anomalies – it limits the maximum differential error to about 0.5 meters. Since the reduced threat model (the "yellow zone" in Figure 8)

is limited to higher-speed anomalies, airborne monitoring is likely to be more effective in practice.

3.4 Results with LGF and Airborne Monitoring

This section includes both LGF and airborne monitoring and thus takes advantage of the better features of both methods. A summary plot is shown in Figure 29. As noted previously, LGF monitoring is superior for speeds of 300 m/s and below, and airborne monitoring is much superior for faster speeds. Since faster speeds are thought to be more likely, airborne monitoring has a significant role to play for Category II/III operations, where it is highly desirable to limit the maximum zenith ionospheric range-domain errors to 0.5 meters or less.

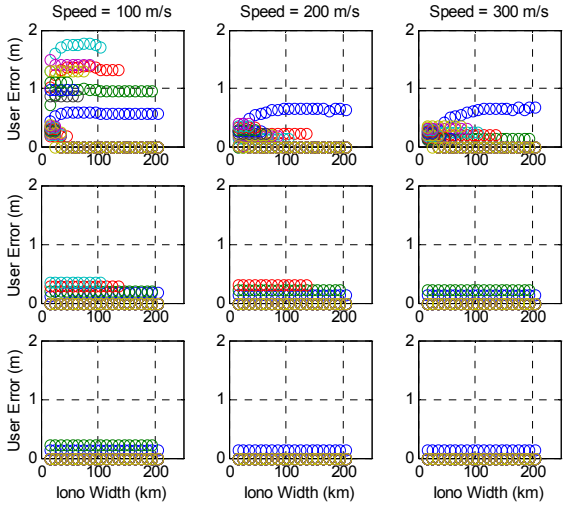

Figure 29: Summary Plots with LGF and Airborne Monitoring

The worst-case anomaly cases for LGF and airborne monitoring are summarized in Table 4. With both LGF and airborne monitoring included, the ionospheric anomaly parameters that give the largest differential range errors vary considerably and are not always at the most severe "edge" of the threat space, although the smallest width (15 km) remains the worst for the "mid-speed" cases between 400 and 700 m/s. Worst-case gradients are much lower than the 400 mm/km maximum because of the impact of monitoring in removing the more extreme gradients quickly. Also, this table makes it clear how airborne monitoring significantly reduces the maximum vertical differential error as the wave front speed increases. Above 500 m/s, this error is below 0.3 meters and is essentially negligible, although airborne detection (and potential loss of continuity) is required to achieve this.

Table 4: Worst-Case Ionospheric Spatial Anomaly Scenarios for Each Wave Front Speed with LGF and Airborne Monitoring

Iono. Front Speed (m/s)	Gradient Slope (mm/km)	Gradient Width (km)	Gradient Direction (deg.)	Worst-Case Diff. Range Error (m)
100	90	75	0	1.8
200	30	135	0	0.7
300	30	195	0	0.7
400	90	15	0	0.4
500	70	15	0	0.3
600	50	15	0	0.2
700	50	15	0	0.2
800	30	195	0	0.1
900	30	145	0	0.1

Table 5 summarizes the ionospheric anomaly cases that give the largest differential errors across three of the four monitor scenarios examined for the case where the LGF-to-threshold (DH) separation is 5 km. As we have noted, the worst-case anomaly differs greatly across these three monitor scenarios, and as monitoring is added, it is more likely that the worst-case anomaly is not at the edge of the threat space. While airborne monitoring is ineffective against low-speed wave fronts, and it does not reduce the worst possible vertical differential range error (across all anomalies within the threat space) below 1.8 meters, it does make that magnitude of error much less likely by being more effective against faster wave front speeds.

Table 5: Worst-Case Ionospheric Spatial Anomaly Scenarios for Three Monitor Scenarios

Monitoring Category	Wave Front Speed (m/s)	Grad. Slope (mm/km)	Grad. Width (km)	Grad. Direction (degree)	Worst-Case Diff. Range Error (m)
No Monitoring	100	400	25	0	7.1 m
LGF Monitoring	600	400	15	0	1.8 m
LGF and Airborne Monitoring	100	90	75	0	1.8 m

Figure 30 shows worst-case differential (vertical) range error (at 5 km LGF-threshold separation) as a function of wave front speed for the three monitor scenarios shown in the table on the previous slide. It graphically points out the advantage airborne monitoring provides in more rapidly detecting anomalies with faster wave front speeds and reducing maximum errors to negligible levels. At speeds at and above 600 m/s, LGF-only monitoring does not reduce the maximum error beyond that of no monitoring at all, but the maximum error in those cases is still less than 2 meters.

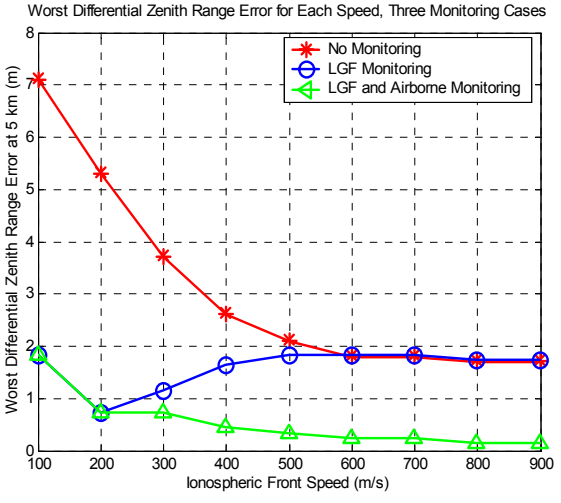

Figure 30: Worst-Case Comparison among Three Monitoring Cases

4.0 POSITION DOMAIN ANALYSIS

In order to translate range-domain errors into position errors, a simulation has been conducted using the satellite geometry visible at Washington, D.C. at the time of passage of the ionosphere anomaly on 6 April 2000. Although it will not necessarily apply to all such anomalies, it is assumed that the wave front in this case moved approximately from North to South. The scenario is illustrated with the sky plot in Figure 31.

For each fixed satellite geometry, we let the ionospheric wave front move from the very north to the very south of the "sky". Only the thin shell ionospheric model is used in the simulation; and the height of the shell is assumed to be 350 km above the surface of the earth. It can be calculated that the distance that the wave front travels is about 4235 km. Each satellite IPP is going to be "hit" by the wave front; one after another. Then the satellite geometry propagates to the next step (in a 10-minute interval), and the wave front sweeps through the "sky" again. Thus, all combinations of satellite geometry in 24 hours and the ionospheric wave front location are considered.

Figure 32 shows the vertical position error for the baseline wave front case. The *x*-axis is the time in hour for satellite geometry. The *y*-axis is the location of the ionospheric wave front. As can be seen, it presents a mountain-like structure. Whenever a satellite IPP is hit, there is a peak of vertical error associated with it. Note that the height of the peak depends on which satellite is impacted and when it is impacted.

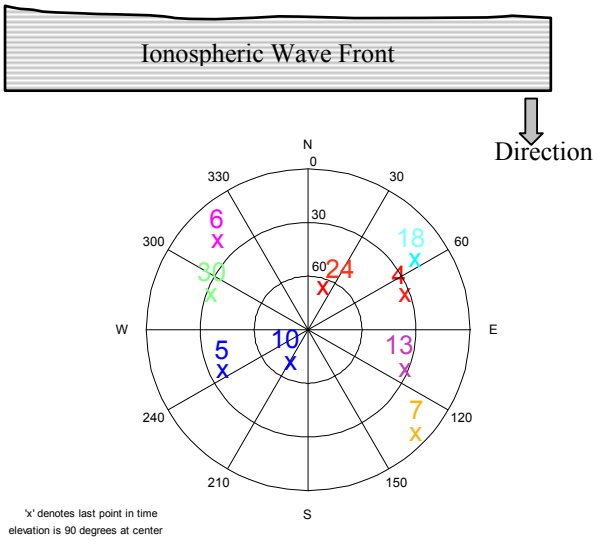

Figure 31: Illustration of Satellite Geometry and Ionospheric Motion

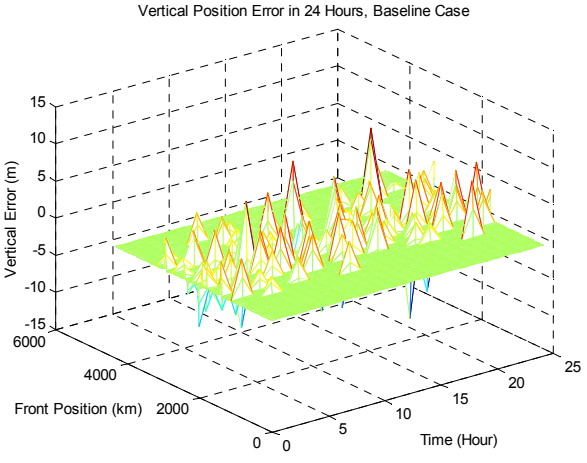

Figure 32: Vertical Position Error for the Baseline Case

In order to show how each variable is cycled through in the simulation, the procedure is depicted in Figure 33. From each point in the threat space, a plot like Figure 32 is generated. The maximum is obtained for that particular

case. Then all the maximums through the entire threat space are collected and summarized in Figure 34. In other words, the points on these plots represent the impact of the ionosphere wave for the worst satellite affected and at the worst time during the 24 hours. No monitoring, LGF monitoring, and both LGF and airborne monitoring are shown in red (row 1), blue (row 2), and green (row 3), respectively. The maximum vertical errors are about 20, 6, and 5 meters for the three monitoring categories.

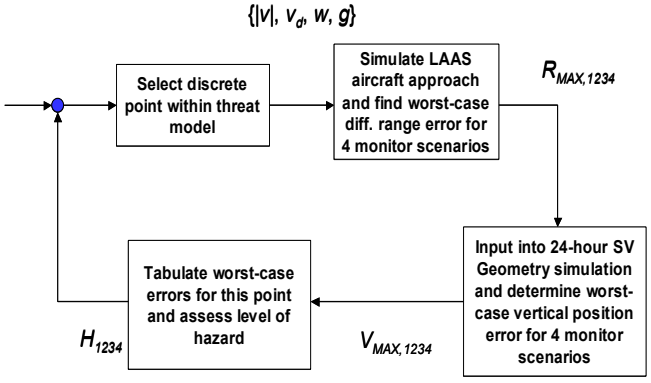

Figure 33: Complete Simulation Procedure for Revised Threat Model

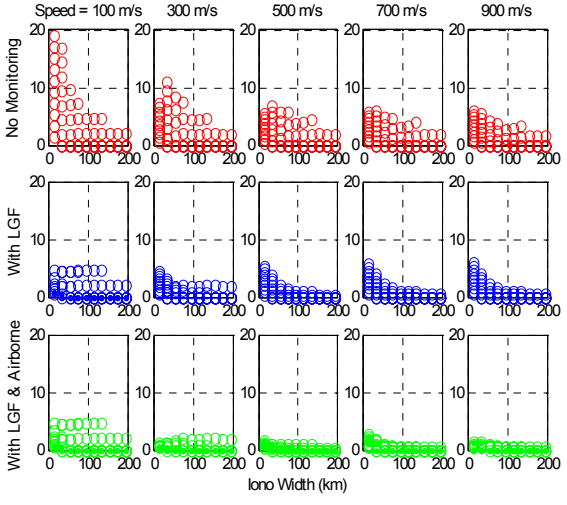

Figure 34: Summary of Maximum Vertical Errors for Three Monitoring Cases

It is useful to put the results into statistical perspective. Figure 35 shows the cumulative distribution (1 – CDF) of all the vertical errors. i.e., the *y*-axis gives the probability of exceeding a given *x*-axis value of differential ionosphere vertical error at 5 km. All points from plots such as Figure 32 (for all cases in the threat space) were included in the histogram that the CDF is based on. The red, blue, green curves represent no monitoring, LGF monitoring, and both LAG and airborne monitoring, respectively. For example, given the presence of an ionospheric storm, the probability of the vertical position error to exceed 10 meter is about 3×10^{-4} with no monitoring. But with both LGF and airborne monitoring, the vertical error will never exceeds 5.3 meters.

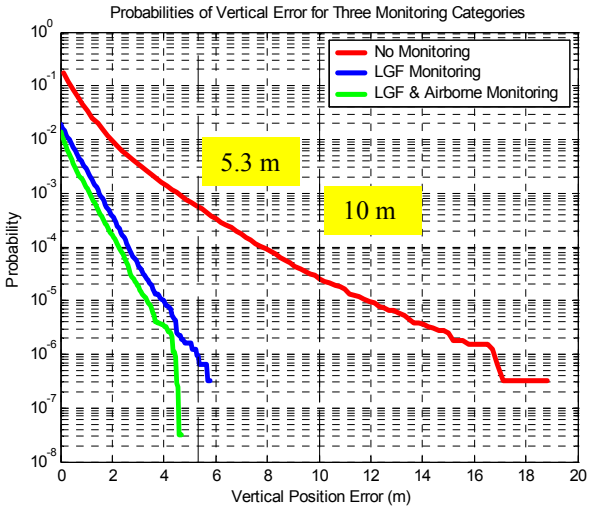

Figure 35: Probability of Vertical Errors

5.0 CONCLUSIONS AND ONGOING WORK

The current version of ionosphere threat model is very broad and contains points that may be physically impossible (or at least very improbable). Our approach to date has been to be conservative and include physically questionable points within the threat model. With more data analysis, it may be possible to exclude physically unrealistic points from the threat model in the future (thereby creating a "reduced" threat model). However, since we will never have perfect physical information about the possible extend of ionosphere anomalies, the upper bounds on ionosphere gradients will remain somewhat arbitrary.

As demonstrated in Section 3.1, the maximum differential error due to spatial ionosphere anomalies is a strong function of maximum distance from the LGF to the threshold (aircraft decision height) for a given approach. For a maximum distance of 5 km, maximum differential errors are significantly less than they would be if this separation distance were not constrained. This presents a new siting constraint, but its impact is likely similar to that of the existing LAAS ephemeris protection levels.

For a given threat model scenario (four anomaly parameters) and LGF-to-threshold distance, a worst-case "timing" (initial position of the airplane and the wave front; two parameters) can be found to maximize differential range error. Without LGF monitoring, the maximum differential range error (5 km maximum

approach distance) is about 7 meters and the vertical position error is about 20 meters. The LGF monitoring capability demonstrated by the Stanford IMT is sufficient to reduce the maximum differential range error (again, for a 5-km maximum approach distance) to about 2 meters and the vertical position error to be about 6 meters. This level of threat mitigation is likely sufficient for Category I precision approaches.

The current model of airborne code-minus-carrier monitor performance is based on the IMT GMA monitor and is probably conservative – a monitor optimized for airborne use will likely have estimation filter time constant much shorter than 200 seconds. With the current model, airborne monitoring does not help against slow (100 m/s or less) wave front speeds. For these cases, LGF monitoring (with about a 2-meter maximum error) still dominates. However, airborne monitoring sharply reduces maximum errors for the (more likely) higher wave speeds. For speeds of 400 m/s or greater, the maximum differential error is about 0.5 m, and this maximum error gets smaller as the speed increases. With both LGF and airborne monitoring, the maximum vertical error is reduced to about 5 meters. Airborne monitoring is likely necessary for Category II/III approaches, depending on the VAL that is selected.

The ongoing effort to better understand and mitigate the ionosphere spatial anomaly threat can be divided into two parts. The first part is to perform data analysis to better determine the credibility of the ionosphere spatial anomaly threat space and the relative likelihood of anomalies within this space. In order to achieve this goal, both recent CONUS ionospheric storms (using IGS data) and similar events in Japan (using the very dense Japan Geodetics reference station network known as GEONET) will be studied. The second part is to identify a threat space that is tolerable to LAAS. Using the outputs of these activities, we will re-assess the ionospheric anomaly threat level to LAAS under the LGF and LGF-plus-airborne monitoring scenarios. The existing worst-case and ensemble (histogram) simulation results will be updated based on the results of the ionosphere data analysis and the revised threat space. The Category I LAAS integrity impact under several integrity requirement definitions will be reviewed to support LGF development and certification decisions.

ACKNOWLEDGMENTS

The authors would like to thank the FAA LAAS Program Office (AND-710) for its support of this research. The opinions expressed here are those of the authors and do not necessarily represent those of the FAA or other affiliated agencies.

REFERENCES

[1] P. Misra, P. Enge, *Global Positioning System: Signals, Measurements, and Performance*. Ganga-Jamuna Press, 2001.

[2] S. Datta-Barua, *et.al*., "Using WAAS Ionospheric Data to Estimate LAAS Short Baseline Gradients," *Proceedings of ION 2002 National Technical Meeting*. Anaheim, CA, January 28-30, 2002, pp. 523-530.

[3] *Specification: Performance Type One Local Area Augmentation System Ground Facility.* Washington, D.C., Federal Aviation Administration, FAA-E-2937A, April 17, 2002.

[4] M. Luo, *et.al*, "Assessment of Ionospheric Impact on LAAS Using WAAS Supertruth Data", *Proceedings of The ION 58th Annual Meeting*. Albuquerque, NM, June 24-26, 2002, pp. 175-186.

[5] T. Dehel, "Ionospheric Wall Observations," Atlantic City, N.J., William J. Hughes FAA Technical Center, FAA ACT-360, February 24, 2003.

[6] G. Xie, *et.al*., "Integrity Design and Updated Test Results for the Stanford LAAS Integrity Monitor Testbed (IMT)," *Proceedings of ION 2001 Annual Meeting*. Albuquerque, NM, June 11-13, 2001, pp. 681-693.

[7] B. Pervan, "A Review of LGF Code-Carrier Divergence Issues", Illinois Institute of Technology, MMAE Dept., May 29, 2001.

[8] G. Xie, *et.al.*, "Detecting Ionospheric Gradients with the Cumulative Sum (CUSUM) Method," Paper AIAA 2003-2415, *Proceedings of 21st International Communications Satellite Systems Conference*, Yokohama, Japan, April 16-19, 2003.

[9] M. Basseville and I. Nikiforov, *Detection of Abrupt Changes – Theory and Application*. Prentice-Hall, ISBN 0-13-126780-9, 1993.

[10] S. Pullen, "Summary of Ionosphere Impact on PT 1 LAAS: Performance and Mitigation Options," Stanford University, Dept. of Aero/Astro, December 14, 2000.

[11] *Minimum Aviation System Performance Standards for Local Area Augmentation System (LAAS)*. Washington, D.C., RTCA SC-159, WG-4A, DO-245, Sept. 28, 1998.

[12] *Minimum Operational Performance Standards for GPS/Local Area Augmentation System Airborne Equipment*. Washington, D.C., RTCA SC-159, WG-4A, DO-253A, Nov. 28, 2001.

[13] *Minimum Operational Performance Standards for GPS/Wide Area Augmentation System Airborne Equipment.* Washington, D.C., RTCA SC-159, WG-2, DO-229C, Nov. 28, 2001.

[14] S. Pullen, B. Pervan, *et.al*., Ephemeris Protection Level Equations and Monitor Algorithms for GBAS, *Proceedings of ION GPS 2001*, Salt Lake City, UT., Sept. 11-14, 2001, pp. 1738-1749.